catalysts

MDPI

Article

Flower-Like Au–CuO/Bi_2WO_6 Microsphere Catalysts: Synthesis, Characterization, and Their Catalytic Performances for CO Oxidation

Lili Wang [1], Baolin Zhu [1,2], Shoumin Zhang [1,2] and Weiping Huang [1,2,3,*]

1 College of Chemistry, Nankai University, Tianjin 300071, China; wangchao19921202@126.com (L.W.); zhubaolin@nankai.edu.cn (B.Z.); zhangsm@nankai.edu.cn (S.Z.)

2 The Key Laboratory of Advanced Energy Materials Chemistry (Ministry of Education), Nankai University, Tianjin 300071, China

3 Collaborative Innovation Center of Chemical Science and Engineering, Tianjin 300071, China

* Correspondence: hwp914@nankai.edu.cn; Tel.: +86-138-2009-6974

Received: 15 August 2017; Accepted: 5 September 2017; Published: 11 September 2017

Abstract: The flower-like Bi_2WO_6 microsphere was synthesized through a simple hydrothermal route, and three catalysts, Au/Bi_2WO_6, CuO/Bi_2WO_6, and Au–CuO/Bi_2WO_6, were prepared by a deposition–precipitation method. The morphology and structure of the catalysts were characterized by X-ray powder diffraction, surface area analyzer, inductively coupled plasma optical emission spectrometer, scanning electron microscope, transmission electron microscopy, UV/Vis spectrometer, as well as X-ray photoelectron spectroscopy. Their catalytic performances in catalytic CO oxidation were evaluated. For Au/Bi_2WO_6 and CuO/Bi_2WO_6, Au and CuO nanoparticles highly dispersed on Bi_2WO_6 are 3 and 10 nm, respectively, in average size. For Au–CuO/Bi_2WO_6, a part of the Au nanoparticles (Au NPs) strongly adheres to the CuO, due to the strong interaction between Au NPs and CuO, which has a positive effect on catalytic activity of Au–CuO/Bi_2WO_6. Au–CuO/Bi_2WO_6 can convert CO into CO_2 completely at 40 °C, as the contents of Au and Cu are 0.438 wt % and 4.85 wt %, respectively.

Keywords: Bi_2WO_6; Au; CuO; CO oxidation; flower-like microsphere

1. Introduction

In recent decades, catalytic CO oxidation has become an important research topic due, to its practical applications in fuel cells, industrial air emission cleaning and automotive exhaust treatment, and so on [1,2]. The catalyst systems for catalytic CO oxidation usually contain noble, nonferrous and ferrous metals, such as Au [3], Pt [4], Pd [5], Cu [6] and Mn [7]. Supported Au nanoparticles (Au NPs) exhibit a remarkable catalytic activity in the catalytic CO oxidation, even at ambient temperature [8]. Theoretically, various factors can affect the activity of supported Au catalysts, including size of Au NPs [9], oxidation state of Au active sites, and synergistic interaction between Au NPs and the support. Especially, highly dispersed Au NPs on support can provide higher activity and stability [10].

CuO, which is apt to change valence state by trapping or releasing surface lattice oxygens [11], has been extensively investigated as a catalyst for catalytic CO oxidation, due its higher catalytic activity and lower cost in comparison with other noble metal catalysts [1]. Besides pure CuO, some composite oxides containing CuO show good activity; for instance, CuO–Fe_2O_3 [12,13], CuO–MnO_2 [2], CuO–Ce_2O_3 [14–17], CuO–TiO_2 [1], CuO–$Ti_xZr_{1-x}O_2$ [18], and CuO–$Ce_xZr_{1-x}O_2$ [19]. The high activities of catalysts containing CuO are usually attributed to the synergy between the Cu species and the support.

In addition, supported bimetallic catalysts, such as Au–Cu [20], Au–Pt [21], and Au–Ag [22], for catalytic CO oxidation, have been investigated. The Au–Cu alloy catalysts are significantly more

active than monometallic Cu and Au catalysts, because there is a synergistic interaction between Cu and Au, and Cu can facilitate the activation of molecular oxygen [23,24]. Zhang et al. reported that Au–Cu alloy nanoparticles highly dispersed in the channels of SBA-15 are highly sintering-resistant even at high temperature treatment, and have much better catalytic performance than monometallic particles in catalytic CO oxidation, due to the synergistic effect between Au and Cu [25]. Jeon et al. investigated the effect of Cu content on the catalytic properties of Au–CuO heterostructured nanocrystals by comparatively examining their performances in catalytic CO oxidation [26]. Carabineiro et al. [27] have reported that Au (1 wt %)/CuO was synthesized by ultrasonication and double impregnation methods, respectively, and the activities for catalytic CO oxidation of catalysts were obtained at room temperature.

Bi_2WO_6 has a layered structure, with the pervoskite-like slab of WO_6 and $[Bi_2O_2]^{2+}$ layers [28–31], which has attracted extensive attention in many research fields because of its excellent characteristics [32]. Recently, Bi_2WO_6 with different morphologies, such as nanoplates [33], nanofibrous [34], nanospheres [35], hierarchical nanostructures [36], porous structures [37], and other complex morphologies, have been prepared. Among them, flower-like Bi_2WO_6 microspheres, with unique structure and morphology, are very suitable for using as a support for supported catalysts. To the best of our knowledge, Bi_2WO_6 has rarely been reported as a support, though it is widely used as a catalyst in photocatalytic reactions.

In the present contribution, flower-like Bi_2WO_6 microspheres and catalysts, Au/Bi_2WO_6, CuO/Bi_2WO_6 and $Au–CuO/Bi_2WO_6$, were synthesized and characterized. Their catalytic activities in catalytic CO oxidation were evaluated.

2. Results and Discussion

2.1. XRD

XRD was firstly used to determine the structure and crystallinity of the as-prepared samples. Figure 1 and Figures S1–S5 show the XRD patterns of all the products. The peaks in all diffraction patterns can be perfectly indexed to the orthorhombic phase of Bi_2WO_6 (JCPDS No. 73-1126) [29], which indicates that hydrothermally synthesized Bi_2WO_6 is of satisfactory purity. The peaks of Au are not apparently visible in Figure 1, Figures S2, S3 and S5. This is probably due to the small particle size and the relatively low concentrations of Au. The peaks at $2\theta = 35.5^\circ$ and 38.7° assigned to diffractions of CuO (002) and (111) (JCPDS No. 45-0937), respectively, are apparently visible in Figure 1, Figures S4 and S5. The XRD patterns also indicate that the prepared samples have high crystallinity. In Figure S1, the intensity of peaks increases with increasing of the calcination temperature, which implies that the calcination is beneficial to the improvement of crystallinity of Bi_2WO_6.

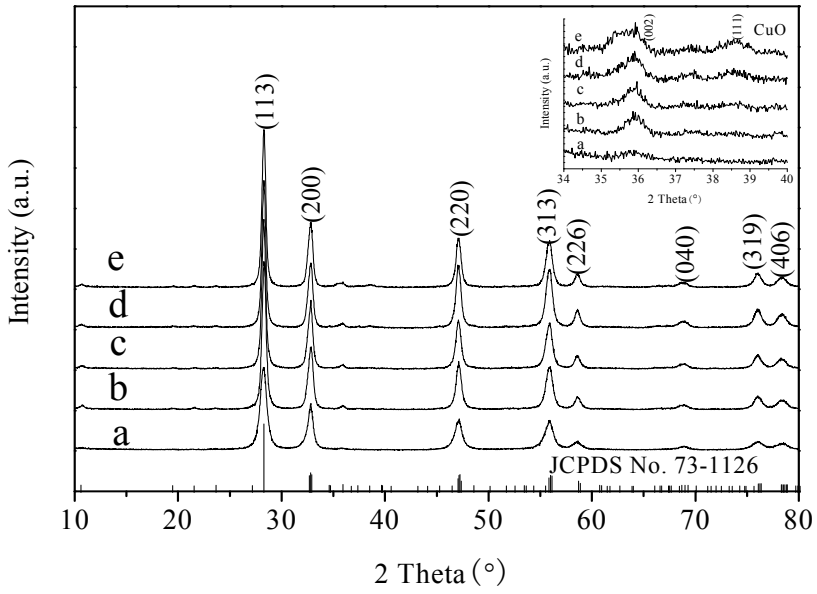

Figure 1. XRD patterns of Bi_2WO_6-400 and (**a**) Au–CuO/Bi_2WO_6-400; (**b**) Cu 1.64 wt %, Au 0.415 wt %; (**c**) Cu 3.27 wt %, Au 0.425 wt %; (**d**) Cu 4.85 wt %, Au 0.438 wt %; (**e**) Cu 6.61 wt % Au 0.448 wt %.

2.2. SEM

The morphology of products was investigated by SEM analysis. As showed in Figure 2a,b, the morphology of Bi_2WO_6 and Bi_2WO_6-400 (Bi_2WO_6 was calcined in air at 400 °C for 2 h) is almost a perfect flower-like microsphere with a diameter of about 2 μm. The microsphere is composed of numerous nanosheets pointing toward the center of the sphere. After calcination, Bi_2WO_6-400 maintains the morphology of microspheres, but the specific surface areas (SSA) of Bi_2WO_6-400 is reduced to 19.35 $m^2 \cdot g^{-1}$ (Bi_2WO_6 is 35.75 $m^2 \cdot g^{-1}$).

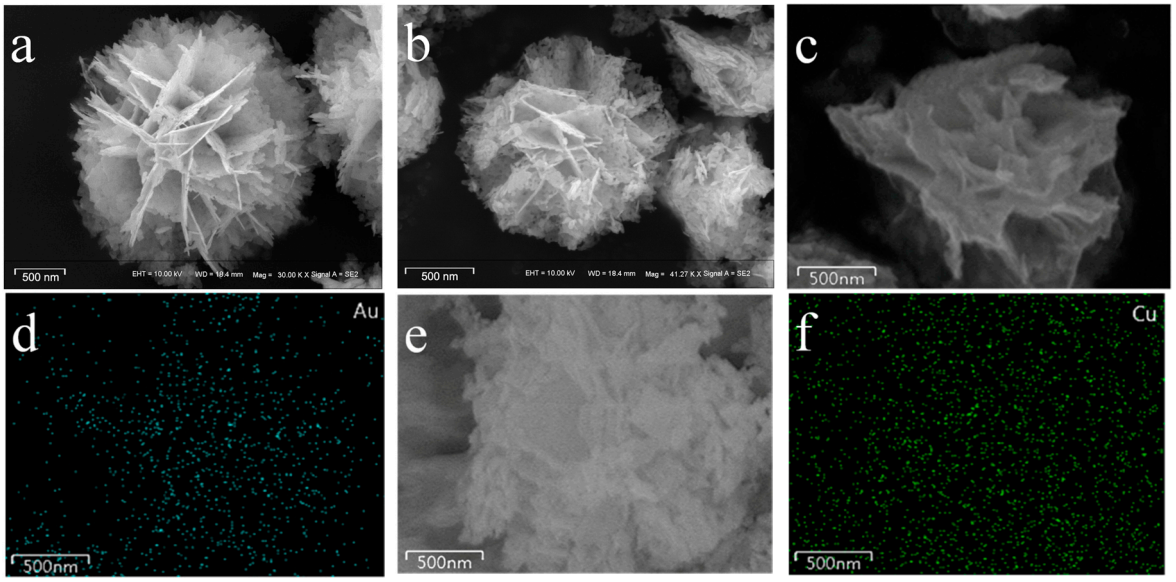

Figure 2. *Cont.*

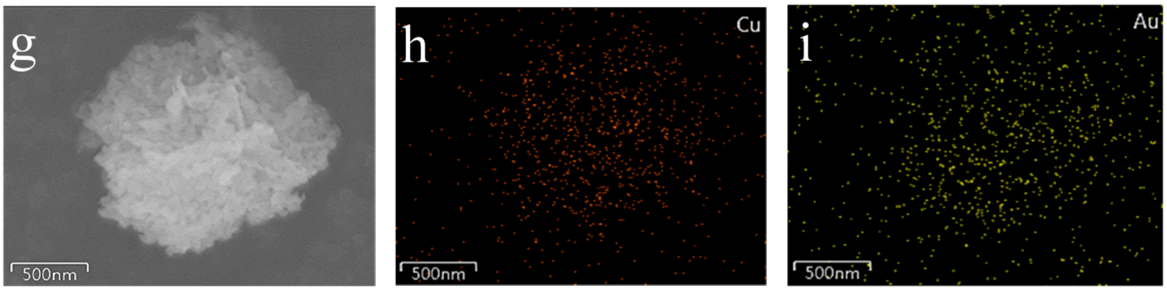

Figure 2. SEM images of Bi_2WO_6 (**a**) and Bi_2WO_6-400 (**b**) SEM images and mapping of the Au/Bi_2WO_6-400 (calcinated at 300 °C): Au 1.30 wt % (**c**,**d**); CuO/Bi_2WO_6-400: Cu 5.10 wt % (**e**,**f**) and Au–CuO/Bi_2WO_6-400: Cu 4.85 wt %, Au 0.438 wt % (**g**–**i**).

It can be seen from Figure 2c,e,g that the morphology of support remains as flower-like microspheres after the deposition and calcination. The mapping images reveal that Au and CuO species are uniformly dispersed on the surface of the Bi_2WO_6-400 support (Figure 2d,f,h,i). The EDX (Figure S6a,b) shows that the contents of Au and Cu on the surface of Au/Bi_2WO_6-400 (Au 1.30 wt %) and CuO/Bi_2WO_6-400 (Cu 5.10 wt %) are 1.67 wt % and 7.80 wt %, respectively, which are higher than the bulk ones determined by ICP. Similarly, the contents of Cu and Au on the surfaces of Au–CuO/Bi_2WO_6-400 (Cu 4.85 wt %, Au 0.438 wt %) are 6.50 wt % and 0.58 wt %, respectively, which are also higher than the bulk contents of Cu and Au determined by ICP. This implies that Au NPs and CuO are enriched on the surface of the sample, which is in favor for utilizing Au NPs and CuO effectively, and catalytic CO oxidation.

2.3. TEM

Figure 3 shows the TEM images of the Au/Bi_2WO_6-400 (Au 1.30 wt %), CuO/Bi_2WO_6-400 (Cu 5.10 wt %) and Au–CuO/Bi_2WO_6-400(Cu 4.85 wt %, Au 0.438 wt %). It can be seen from Figure 3a,c,e that the support has nearly the same morphology, and the size of flower-like microspheres is still around 2 μm, which agrees with the results of SEM analyses (Figure 2c,e,g). Figure 3b,d,f are the HRTEM images of Figure 3a,c,e. As shown in Figure 3b, Au NPs, ca. 3 nm in size, are uniformly dispersed on the surface of Bi_2WO_6-400. As reported in the literature [38], the Au NPs with diameters lower than 5 nm are critical for the high catalytic activity of the supported Au catalysts. In this work, the size of uniform spherical Au NPs is about 3 nm after calcination at 300 °C. In Figure 3d, it is clear that CuO particles with the diameter of 10 nm are uniformly dispersed on the support surface. The plane fringe with a crystalline plane spacing of 0.253 nm is assigned to the (002) plane of CuO [39]. In Figure 3f, the interplanar distances of 0.235 and 0.253 nm correspond to the spacing of the (111) plane of Au and (002) plane of CuO. Au NPs and CuO are uniformly dispersed on the surface of the support. However, compared with Figure 3b,d, the edge of the particles in Figure 3f is not clear, the size of the particles is reduced, and a part of Au NPs strongly adhere to the CuO. These results provide clear evidence that there is a synergetic effect between Au NPs and CuO. Thus, it can affect the catalytic activity of the catalyst.

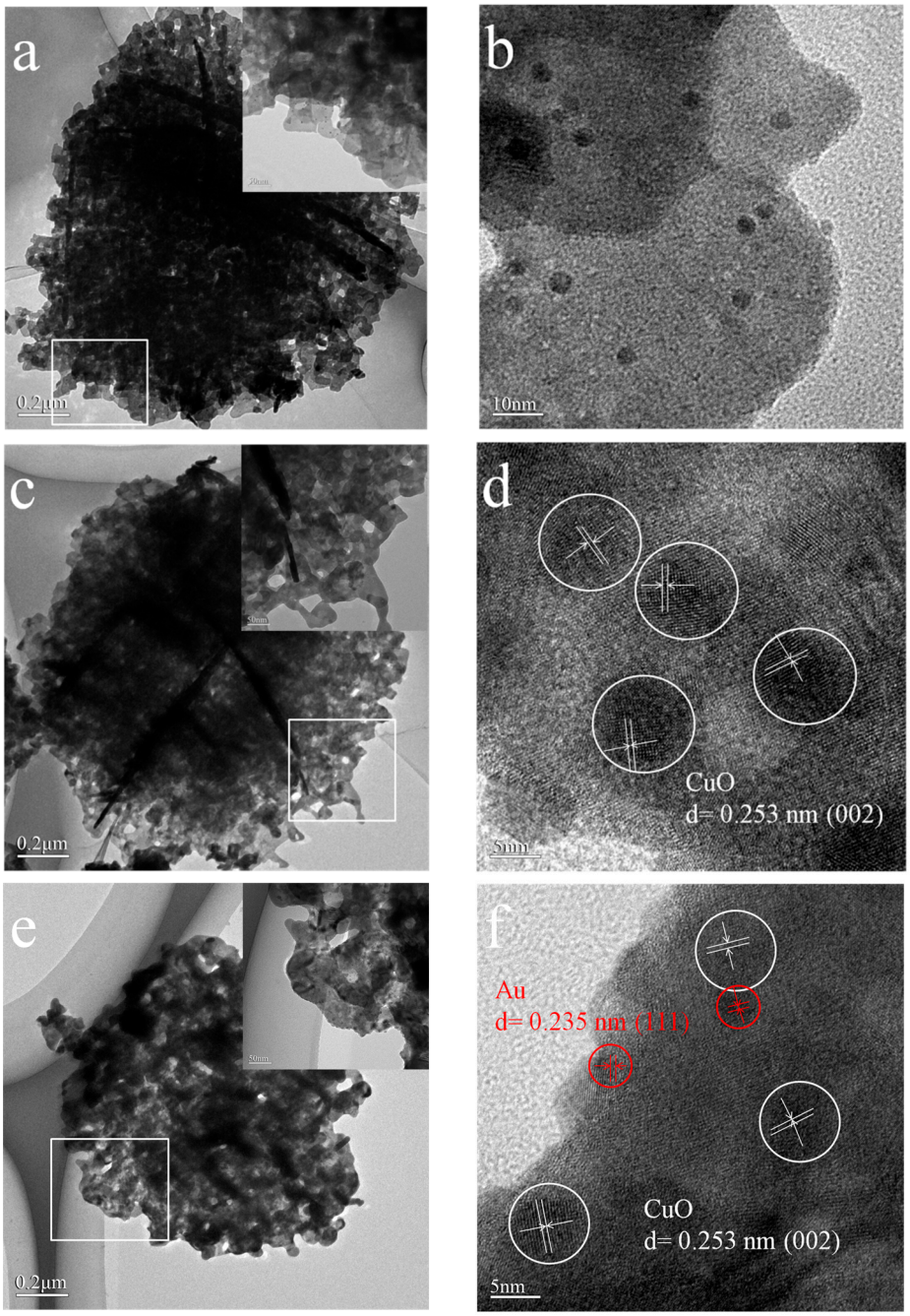

Figure 3. TEM images of the Au/Bi_2WO_6-400 (calcinated at 300 °C): Au 1.30 wt % (**a**,**b**); CuO/Bi_2WO_6-400: Cu 5.10 wt % (**c**,**d**) and Au–CuO/Bi_2WO_6-400: Cu 4.85 wt %, Au 0.438 wt % (**e**,**f**).

2.4. UV–Vis Spectra

The diffuse reflectance UV–vis spectra of Bi_2WO_6, Bi_2WO_6-400 and Au/Bi_2WO_6-400 calcined at different temperatures are presented in Figure 4. As shown in Figure 4, the absorption edge of Bi_2WO_6 and Bi_2WO_6-400 is at about 448 nm, which suggests that the support absorbs visible light weakly. Compared with the spectra of the support, the spectra of the catalysts calcined at different temperatures exhibits obvious and broad absorption bands between 500 and 700 nm, which is due to the surface plasmon resonance (SPR) of metallic Au NPs. The presence of a plasmon band is ascribed to the collective oscillation of conduction electrons in response to optical excitation, and is affected by the shape and size of the dispersed Au NPs, as well as the dielectric properties of the

surrounding material. There are several reasons for the shift of the absorption band. One is that for small clusters (diameter <2 nm), the absorption band is red-shifted and broadened, owing to size-dependent damping of the metal dielectric function. Another is that leading to a red shift is a reduction of electron density in the gold particles, owing to chemical interactions with the surrounding metal oxides, favoring the transition of electrons from the cluster to the surrounding matrix. The red shift of SPR peaks in Figure 4 implies that the size of Au NPs increased, or the interaction between Au and Bi_2WO_6-400 was strengthened with the increase of calcination temperature.

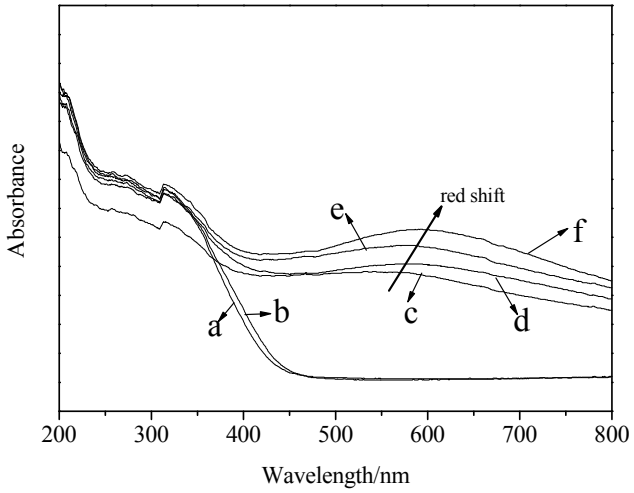

Figure 4. The diffuse reflectance UV–vis spectra of Bi_2WO_6 (**a**); Bi_2WO_6-400 (**b**) and Au/Bi_2WO_6-400 calcined at different temperatures: 80 °C (**c**); 200 °C (**d**); 300 °C (**e**); 400 °C (**f**).

2.5. XPS Spectra

XPS was further performed to investigate the surface chemical composition and chemical states of the samples. Figure 5, Figures S7 and S8, show the XPS spectra of Au–CuO/Bi_2WO_6-400 (Cu 4.85 wt %, Au 0.438 wt %), Au/Bi_2WO_6-400 (Au 1.30 wt %) and CuO/Bi_2WO_6-400 (Cu 5.10 wt %). In Figure 5a, the peaks at 158.9 eV and 164.1 eV can be ascribed to Bi $4f_{7/2}$ and Bi $4f_{5/2}$ of Bi^{3+} species in Bi_2WO_6, respectively. As shown in Figure 5b, the two peaks at 37.5 and 35.4 eV are assigned to W $4f_{5/2}$ and W $4f_{7/2}$, respectively, which are the features of W^{6+} species in the WO_6 octahedron. The O 1s peak could be fitted into two peaks (Figure 5c), positioned at 529.8 and 532.2 eV, which are assigned to crystal lattice oxygen $[Bi_2O_2]^{2+}$ and $[WO_4]^{2-}$ layers of Bi_2WO_6 and the adsorbed oxygen, in the form of hydrated species OH on the surface, respectively. Figure 5d presents the XPS spectra of Cu 2p of the catalyst. It has been well established that the presence of a shake-up peak at about 940–945 eV, and the Cu $2p_{3/2}$ binding energy at 933.0–933.8 eV, are two major XPS characteristics of CuO [12,18,40]. The characteristic peaks of Au $4f_{7/2}$ and Au $4f_{5/2}$ spin-orbital splitting photoelectrons are located at 84.0 and 87.5 eV (Figure 5e), which is characteristic for zero valent gold [41]. For catalysts, the presence of metallic Au might benefit the catalytic performance in the catalytic CO oxidation. The binding energy of oxidized gold species, which should be located at around 85.5 and 86.3 eV [41], has been not detected. The Au-content of Au/Bi_2WO_6-400: Au 1.30 wt % (300 °C), the Cu-content of CuO/Bi_2WO_6-400: Cu 5.10 wt %, and Cu-content and Au-content of Au–CuO/Bi_2WO_6-400 (Cu 4.85 wt %, Au 0.438 wt %) detected by XPS, is listed in Tables S1–S3, respectively. The surface Au-content and Cu-content were higher than the content determined by ICP, indicating the Au NPs and CuO mostly dispersed on the surface of Bi_2WO_6-400.

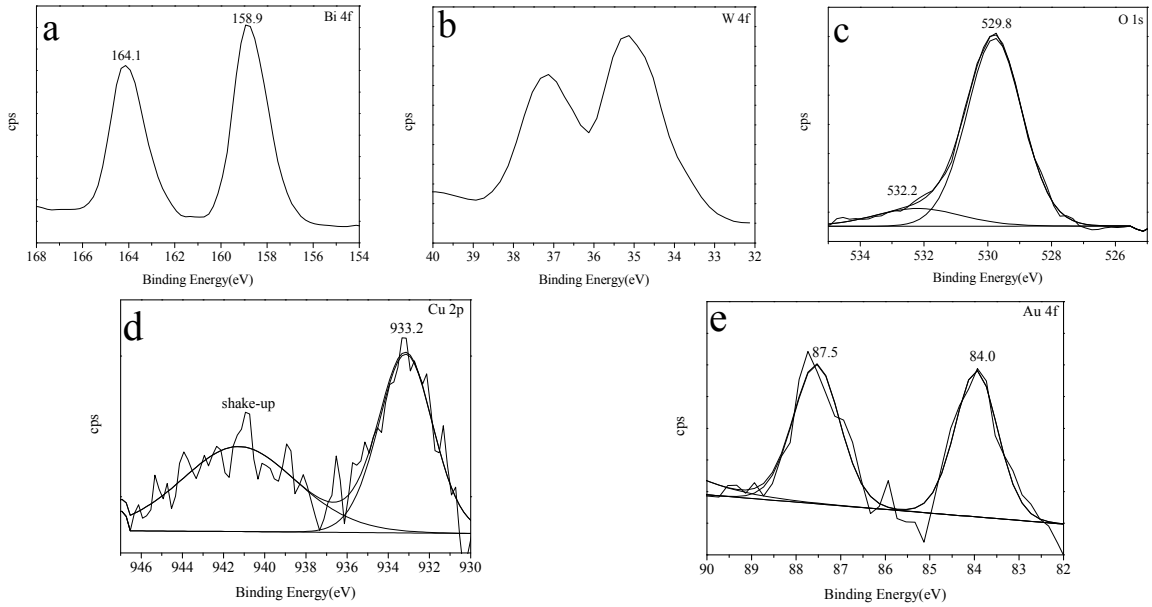

Figure 5. XPS spectra of Au–CuO/Bi_2WO_6-400 (Cu 4.85 wt %, Au 0.438 wt %): Bi 4f peaks (**a**); W 4f peaks (**b**); O 1s peaks (**c**); Cu 2p peaks (**d**); Au 4f peaks (**e**).

However, the XPS spectra of Bi (Figure 5a, Figures S7a and S8a and W (Figure 5b, Figures S7b and S8b) are modified after Au and Cu deposition. The shifts of peaks (Figure 5e vs. Figure S7d, Figure 5d vs. Figure S8d) indicate that some charges might be transferred to Au and CuO species on the surface of Bi_2WO_6-400. It can be deduced that there might exist strong interactions among Au, CuO, and Bi_2WO_6-400, which might change the electronic properties of Au and CuO.

2.6. Catalytic Activity Studies

The catalytic activities of catalysts for catalytic CO oxidation were evaluated. All the catalysts showed high catalytic activities, but the support showed no activity. It is worth pointing out that in this contribution, the gas used contained 10% CO, while in most studies, the gas used contained 1% CO. Figure 6 shows the catalytic activities of Au/Bi_2WO_6 and Au/Bi_2WO_6-400 with different Au-contents. It can be seen from the Figure 6 that the catalytic activity of the catalyst increased with the increasing of Au-content, which is not dependent on the support. When the Au-content is similar, the catalytic activity of Au/Bi_2WO_6-400 is higher than that of Au/Bi_2WO_6.

Figure 7 depicts the catalytic activities of Au/Bi_2WO_6-400 (Au 1.30 wt %) calcined at different temperatures. It can be found that the calcination temperature significantly affected the activity of catalyst. The catalytic activity of catalyst increased with the raising of calcination temperature (from 80 to 300 °C). Over Au/Bi_2WO_6-400 (Au 1.30 wt %) calcined at 300 °C, the conversions of CO at 10 °C and 30 °C are about 50% and 100%, respectively. The high catalytic activity should come from the small Au particles of 3 nm, as seen in the TEM images (Figure 3b). However, for catalyst calcinated at 400 °C, the conversion of CO decreased obviously, and the percent conversion of CO was zero at 30 °C. Compared with $T_{100\%}$ (30 °C) of Au/Bi_2WO_6-400 (Au 1.30 wt %, 300 °C), that of the Au/Bi_2WO_6-400 (Au 1.30 wt %, 400 °C) was higher (140 °C). It might be reasonably explained by the fact that the size of Au NPs increased greatly (ca. 13 nm) after calcination at 400 °C (Figure S9), which resulted in the decrease of active sites in catalyst. It can be concluded that 300 °C was the optimal calcination temperature.

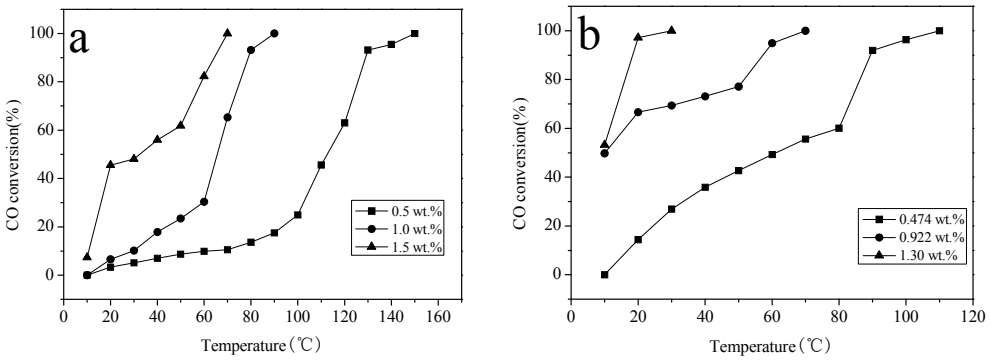

Figure 6. Catalytic activities of Au/Bi_2WO_6 (**a**) and Au/Bi_2WO_6-400 (**b**) with different Au-contents (calcinated at 300 °C).

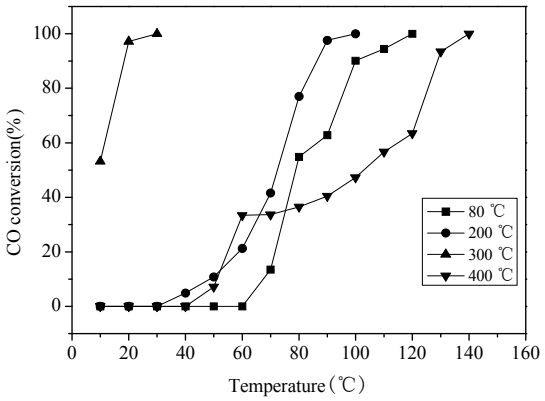

Figure 7. Catalytic activities of Au/Bi_2WO_6-400 (Au 1.30 wt %) calcined at different temperatures.

For all Bi_2WO_6-supported Au catalysts, only Au^0 was identified by XPS. Therefore, it can be concluded that the active sites of catalysts containing Au for CO oxidation are Au^0 species.

The catalytic activities of CuO/Bi_2WO_6 and CuO/Bi_2WO_6-400 with different Cu-contents are shown in Figure 8. Their catalytic activities enhanced with the increase of CuO content in the range of 1.9–5.5 wt %, but decreased with the further increasing CuO content. When the Cu-content is lower than 5.5 wt %, the surface area of the support is large enough for metal or oxide particles to highly disperse, forming highly efficient catalysts. However, as the loading of CuO is higher, the excess CuO species would be aggregated, forming bulk CuO particles, which may reduce the number of active sites, and as a result, make a negative effect on the catalytic activity of catalyst [12].

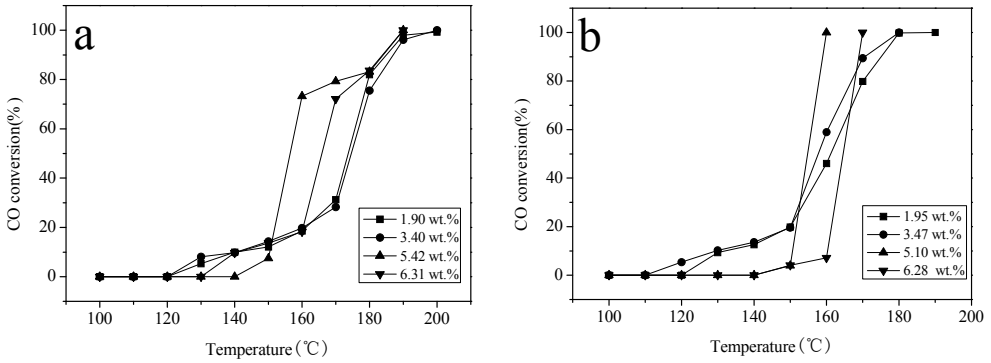

Figure 8. Catalytic activities of CuO/Bi_2WO_6 (**a**) and CuO/Bi_2WO_6-400 (**b**) with different Cu-contents.

It is well known that bulk CuO shows almost no catalytic activity for catalytic CO oxidation when the reaction temperature is below 200 °C [42,43]. However, here, both CuO/Bi_2WO_6 and CuO/Bi_2WO_6-400 exhibit catalytic activity below 200 °C. The result means that structure of the flower-like Bi_2WO_6 can efficiently improve the dispersion of copper species, and Bi_2WO_6 should be a potential support of catalysts for catalytic oxidation reaction.

Compared with Figure 8, Figure 9 shows that the Au–CuO/Bi_2WO_6 and Au–CuO/Bi_2WO_6-400 have an enhanced catalytic activity, and the catalytic performance should be related not only to the size of Au and CuO particles, but also to the synergetic effect between Au and CuO. XPS results show that the binding energy of Au and Cu 2p in catalysts shifts, which originates from the interaction between Au and CuO. Furthermore, after calcination, a part of the Au NPs is strongly adhered to the CuO (Figure 3f), which may lead to the extended interface between Au and CuO. As a result, the Bi_2WO_6-supported Au–CuO catalysts exhibit higher catalytic activity than Bi_2WO_6-supported CuO catalysts.

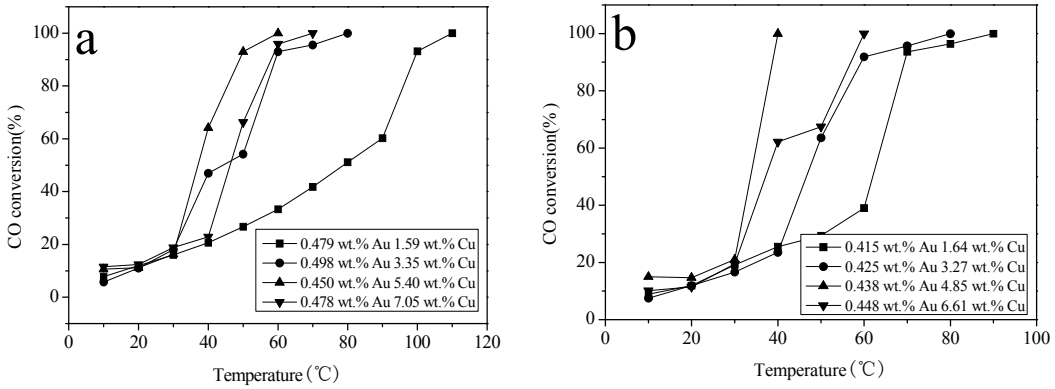

Figure 9. Catalytic activities of Au–CuO/Bi_2WO_6 (**a**) and Au–CuO/Bi_2WO_6-400 (**b**).

Compared to all the samples we prepared, as the contents of Cu and Au were 4.85 wt % and 0.438 wt %, respectively, the catalyst showed the best catalytic performance, over which the CO was turned into CO_2 completely at 40 °C.

The results of Figures 6, 8 and 9 suggest that supports play very important roles in catalytic CO oxidation. The flower-like Bi_2WO_6 microspheres perform the following functions: (1) their unique structure and morphology could greatly enhance the active surface area for adsorbing and stabilizing Au and CuO particles [44]; (2) they store and release oxygen, which provokes higher active oxygen mobility and diffusion from the lattice to the interface of Au NPs and CuO; and (3) the higher crystalline phases of calcined support could improve CO oxidation reduction [33].

3. Experimental

3.1. Synthesis of Flower-Like Bi_2WO_6 Microspheres

The preparation procedures of the flower-like Bi_2WO_6 microspheres are as follows. Firstly, 0.1649 g of $Na_2WO_4{\cdot}2H_2O$ was dissolved in 40 mL solvent mixture (8 mL acetic acid and 32 mL distilled water), forming a clear solution. Then, 0.4851 g of $Bi(NO_3)_3{\cdot}5H_2O$ solid was added to the solution, and a white precipitate appeared. After the precipitation was stirred for 1 h, the resulting slurry was transferred into a 100 mL Teflon-lined stainless steel autoclave, and the autoclave was maintained at 160 °C for 12 h in an oil bath. After cooling naturally to ambient temperature, the solid product in the autoclave was collected, washed, and dried at 80 °C in an oven for 12 h (Bi_2WO_6). The dried precipitation was calcined in air at 400 °C for 2 h (Bi_2WO_6-400).

3.2. Synthesis of Au/Bi_2WO_6

Flower-like Bi_2WO_6 (or Bi_2WO_6-400) microspheres (0.4 g) were dispersed in 100 mL deionized water. The suspension was kept stirred, to make sure microspheres could disperse well. $HAuCl_4$ solution (0.01 mol/L) was added to the above suspension at different volumes. The pH of the suspension was 7–8. After low-energy sonication for 10 min, the suspension was stirred at room temperature for 12 h, and then refluxed for 2 h. The suspension was centrifuged and washed with deionized water to remove adsorbed ions on the outer surface. After drying at 80 °C overnight, the precipitation was calcined at different temperature (200 °C, 300 °C, or 400 °C) for 2 h, respectively.

3.3. Synthesis of CuO/Bi_2WO_6

Flower-like Bi_2WO_6 (or Bi_2WO_6-400) microspheres (0.4 g) were dispersed in 100 mL deionized water. Then, a certain amount of $Cu(NO_3)_2{\cdot}3H_2O$ was added into the above suspension. After that, 0.05 mol/L Na_2CO_3 solution was added to adjust pH value of the final solution to 5–6. After low-energy sonication for 0.5 h, the suspension was stirred at room temperature for 0.5 h. Then, the suspension was centrifuged and washed with deionized water. After drying at 80 °C overnight, the precipitation was calcined at 400 °C for 2 h.

3.4. Synthesis of $Au–CuO/Bi_2WO_6$

The synthesis procedures were like that of Au/Bi_2WO_6, except that the Bi_2WO_6 was replaced by CuO/Bi_2WO_6, and that the samples were calcined at 300 °C for 2 h.

3.5. Characterization

The X-ray powder diffraction (XRD) experiments were carried out at room temperature using a Rigaku D/Max-2500 X-ray diffractometer (Rigaku Corporation, Akishima, Japan) (Cu$K\alpha$ λ = 0.154 nm) in the range of 10–80° to identify the crystallographic phase of samples. The specific surface area was determined at −196 °C using Micromeritics' TriStar II 3020 surface area analyzer (Micromeritics, Atlanta, GA, USA), and calculated using the Brunauer–Emmett–Teller (BET) model. Elemental analysis was performed on an IRIS Intrepid model inductively coupled plasma optical emission spectrometer (ICP-OES) (Thermo, Waltham, MA, USA). The contents of Au and Cu were expressed as wt %. The morphologies of samples were observed using ZEISS MERLIN Compact (Field Emission) X-650 scanning electron microscope (SEM) (Zeiss, Jena, Germany) operating at 25 kV. The samples containing Au were not coated with gold. Transmission electron microscopy (TEM) images were obtained using JEM-2010FEF (Jeol, Akishima, Japan) working at 200 kV. The UV–vis absorption determination of the samples was performed on UV–vis DRS (UV3600 UV/Vis spectrometer) (Shimadzu, Kyoto, Japan). The chemical composition and oxidation state of elements on the surface of samples were identified by X-ray photoelectron spectroscopy (XPS) (Ulvac-Phi, Chigasaki, Japan) using an Al X-ray source (Al $K\alpha$ 150 W, PHI 5000 Versa Probe), and the binding energy was calibrated by taking C 1s peak at 284.6 eV as reference.

3.6. Evaluation of Catalytic Performance of Catalysts for Catalytic CO Oxidation

Evaluation of catalytic performance of catalysts for CO oxidation was performed as the previous report [45]. The experiment was carried out in a fixed-bed flow reactor under atmospheric pressure using 200 mg catalyst. A stainless steel tube with an inner diameter of 8 mm was chosen as the reactor tube. The samples were diluted with 17.6 g chemically inert quartz sand. Subsequently, reaction gas mixture consisting of 10% CO balanced with air was passed through the catalyst bed at a total flow rate of 36.3 mL min^{-1}. The temperature dependence of the sample catalytic activity was recorded in the range of 10–200 °C at a ramping rate of 10 °C min^{-1}. After holding at the reaction temperature for 30 min, effluent gases were analyzed online by GC-508A gas chromatography (Kechuang, Shanghai,

China). The activity was expressed by the percent conversion of CO, which was calculated according to the following equation:

Percent conversion of CO = $\frac{[CO_2]}{[CO] + [CO_2]} \times 100\%$, where [CO] and [$CO_2$] represent the outlet CO and CO_2 concentration, respectively.

4. Conclusions

In summary, the orthorhombic phase flower-like Au/Bi_2WO_6, CuO/Bi_2WO_6, and Au–CuO/Bi_2WO_6 microsphere catalysts have been successfully prepared by a simple deposition–precipitation method. They are excellent catalysts for catalytic CO oxidation. Among the prepared catalysts, Au–CuO/Bi_2WO_6-400 (Cu 4.85 wt %, Au 0.438 wt %) possesses the best catalytic activity, and it can convent CO to CO_2 completely at 40 °C. The flower-like Bi_2WO_6 might be a good support, and the strong interaction between Au and CuO species has a great promoting effect on activity of the catalysts.

Supplementary Materials: The following are available online at www.mdpi.com/2073-4344/7/9/266/s1, Figure S1: XRD patterns of Bi_2WO_6 and Bi_2WO_6-400 supports, Figure S2: XRD patterns of Au/Bi_2WO_6 (a) and Au/Bi_2WO_6-400 (b) with different Au-content, Figure S3: XRD patterns of Au/Bi_2WO_6-400 was calcined at different temperatures, Figure S4: XRD patterns of CuO/Bi_2WO_6 (a) and CuO/Bi_2WO_6-400 (b) with different Cu-content, Figure S5: XRD patterns of Bi_2WO_6 (a), Au–CuO/Bi_2WO_6 (b) Cu 1.64 wt %, Au 0.415 wt %; (c) Cu 3.27 wt %, Au 0.425 wt %; (d) Cu 4.85 wt %, Au 0.438 wt %; (e) Cu 6.61 wt %, Au 0.448 wt %, Figure S6: EDX of the Au/Bi_2WO_6-400: Au 1.30 wt % (a) CuO/Bi_2WO_6–C: Cu 5.10 wt % (b) and Au–CuO/Bi_2WO_6–C: Cu 4.85 wt %, Au 0.438 wt % (c), Figure S7: XPS spectra of Au/Bi_2WO_6-400: Au 1.30 wt % (300 °C): Bi 4f peaks (a); W 4f peaks (b); O 1s peaks (c); Au 4f peaks (d), Figure S8: XPS spectra of CuO/Bi_2WO_6-400: Cu 5.10 wt %: Bi 4f peaks (a); W 4f peaks (b); O 1s peaks (c); Cu 2p peaks (d), Figure S9: TEM image of Au/Bi_2WO_6-400 (calcinated at 400 °C): Au 1.30 wt %, Table S1: The flower-like Au/Bi_2WO_6 microspheres catalysts, Table S2: The flower-like CuO/Bi_2WO_6 microspheres catalysts; Table S3 The flower-like Au-CuO/Bi_2WO_6 microspheres catalysts.

Acknowledgments: This work is supported by the National Natural Science Foundation of China (21373120, 21301098, 21406120 and 21071086).

Author Contributions: Lili Wang performed the experiments; Baolin Zhu, Shoumin Zhang and Weiping Huang conceived the concept. All the authors contributed to the writing of the manuscript.

Conflicts of Interest: The authors declare no conflict of interest.

References

1. Lu, J.Q.; Sun, C.X.; Li, N.; Jia, A.P.; Luo, M.F. Kinetic study of CO oxidation over CuO/MO_2 (M = Si, Ti and Ce) catalysts. *Appl. Surf. Sci.* **2013**, *287*, 124–134. [CrossRef]
2. Qian, K.; Qian, Z.X.; Hua, Q.; Jiang, Z.Q.; Huang, W.X. Structure-activity relationship of CuO/MnO_2 catalysts in CO oxidation. *Appl. Surf. Sci.* **2013**, *273*, 357–363. [CrossRef]
3. Deng, X.Q.; Zhu, B.; Li, X.S.; Liu, J.L.; Zhu, X.B.; Zhu, A.M. Visible-light photocatalytic oxidation of CO over plasmonic Au/TiO_2: Unusual features of oxygen plasma activation. *Appl. Catal. B Environ.* **2016**, *188*, 48–55. [CrossRef]
4. Tomita, A.; Shimizu, K.; Tai, Y. Effect of metal oxide promoters on low temperature CO oxidation over water-pretreated Pt/alumina catalysts. *Catal. Lett.* **2014**, *144*, 1689–1695. [CrossRef]
5. Wang, C.; Wen, C.; Lauterbach, J.; Sasmaz, E. Superior oxygen transfer ability of Pd/MnO_x–CeO_2 for enhanced low temperature CO oxidation activity. *Appl. Catal. B Environ.* **2017**, *206*, 1–8. [CrossRef]
6. Inui, T.; Ono, Y.; Takagi, Y.; Kim, J.B. Oxygen spillover effects induced by Rh-modification on the low-temperature oxidation of CO over Cu-incorporated zeolite A studied by the forced oscillating reaction method. *Appl. Catal. A Gen.* **2000**, *202*, 215–222. [CrossRef]
7. Margitfalvi, J.L.; Hegedúś, M.; Szegedi, Á.; Sajó, I. Modification of Au/MgO catalysts used in low temperature CO oxidation with Mn and Fe. *Appl. Catal. A Gen.* **2004**, *272*, 87–97. [CrossRef]
8. Li, S.N.; Zhu, H.Q.; Qin, Z.F.; Wang, G.F.; Zhang, Y.G.; Wu, Z.W.; Li, Z.K.; Chen, G.; Dong, W.W.; Wu, Z.H.; et al. Morphologic effects of nano CeO_2-TiO_2 on the performance of Au/CeO_2-TiO_2 catalysts in low-temperature CO oxidation. *Appl. Catal. B Environ.* **2014**, *144*, 498–506. [CrossRef]
9. Haruta, M.; Kobayashi, T.; Sano, H.; Yamada, N. Novel gold catalysts for the oxidation of carbon-monoxide at a temperature far below 0 °C. *Chem. Lett.* **1987**, *2*, 405–408. [CrossRef]

10. Albadi, J.; Alihoseinzadeh, A.; Razeghi, A. Novel metal oxide nanocomposite of Au/CuO–ZnO for recyclable catalytic aerobic oxidation of alcohols in water. *Catal. Commun.* **2014**, *49*, 1–5. [CrossRef]
11. Harzandi, A.M.; Tiwari, J.N.; Lee, H.S.; Jeon, H.; Cho, W.J.; Lee, G.; Baik, J.; Kwak, J.H.; Kim, K.S. Efficient CO oxidation by 50-facet Cu_2O nanocrystals coated with CuO nanoparticles. *ACS Appl. Mater. Interface* **2017**, *9*, 2495–2499. [CrossRef] [PubMed]
12. Cao, J.L.; Wang, Y.; Yu, X.L.; Wang, S.R.; Wu, S.H.; Yuan, Z.Y. Mesoporous CuO–Fe_2O_3 composite catalysts for low-temperature carbon monoxide oxidation. *Appl. Catal. B Environ.* **2008**, *79*, 26–34. [CrossRef]
13. Said, A.E.A.A.; El-Wahab, M.M.M.A.; Goda, M.N. Synthesis and characterization of pure and (Ce, Zr, Ag) doped mesoporous CuO-Fe_2O_3 as highly efficient and stable nanocatalysts for CO oxidation at low temperature. *Appl. Surf. Sci.* **2016**, *390*, 649–665. [CrossRef]
14. Zheng, X.C.; Zhang, X.L.; Wang, X.Y.; Wang, S.R.; Wu, S.H. Preparation and characterization of CuO/CeO_2 catalysts and their applications in low-temperature CO oxidation. *Appl. Catal. A Gen.* **2005**, *295*, 142–149. [CrossRef]
15. Zhu, P.F.; Li, J.; Zuo, S.F.; Zhou, R.X. Preferential oxidation properties of CO in excess hydrogen over CuO–CeO2 catalyst prepared by hydrothermal method. *Appl. Surf. Sci.* **2008**, *255*, 2903–2909. [CrossRef]
16. Zeng, S.H.; Chen, T.J.; Liu, K.W.; Su, H.Q. Promotion effect of metal oxides on inverse CeO_2/CuO catalysts for preferential oxidation of CO. *Catal. Commun.* **2014**, *45*, 16–20. [CrossRef]
17. Zeng, S.H.; Zhang, W.L.; Śliwa, M.; Su, H.Q. Comparative study of CeO_2/CuO and CuO/CeO_2 catalysts on catalytic performance for preferential CO oxidation. *Int. J. Hydrog. Energy* **2013**, *38*, 3597–3605. [CrossRef]
18. Huang, J.; Kang, Y.F.; Wang, L.W.; Yang, T.L.; Wang, Y.; Wang, S.R. Mesoporous CuO/TixZr$_{1-x}$O$_2$ catalysts for low-temperature CO oxidation. *Catal. Commun.* **2011**, *15*, 41–45. [CrossRef]
19. Ayastuy, J.L.; Gurbani, A.; Gonźalez-Marcos, M.P.; Gutiérrez-Ortiz, M.A. CO oxidation on CexZr$_{1-x}$O$_2$-supported CuO catalysts: Correlation between activity and support composition. *Appl. Catal. A Gen.* **2010**, *387*, 119–128. [CrossRef]
20. Gamboa-Rosales, N.K.; Ayastuy, J.L.; Boukha, Z.; Bion, N.; Duprez, D.; Pérez-Omil, J.A.; del Río, E.; Gutiérrez-Ortiz, M.A. Ceria-supported Au-CuO and Au–Co_3O_4 catalysts for CO oxidation: An 18O/16O isotopic exchange study. *Appl. Catal. B Environ.* **2015**, *168*, 87–97. [CrossRef]
21. Pongstabodee, S.; Monyanon, S.; Luengnaruemitchai, A. Applying a face-centered central composite design to optimize the preferential CO oxidation over a PtAu/CeO_2–ZnO catalyst. *Int. J. Hydrog. Energy* **2012**, *37*, 4749–4761. [CrossRef]
22. Liu, X.Y.; Wang, A.Q.; Yang, X.F.; Zhang, T.; Mou, C.Y.; Su, D.S.; Li, J. Synthesis of thermally stable and highly active bimetallic Au–Ag nanoparticles on inert supports. *Chem. Mater.* **2009**, *21*, 410–418. [CrossRef]
23. Sandova, A.; Louis, C.; Zanella, R. Improved activity and stability in CO oxidation of bimetallic Au–Cu/TiO_2 catalysts prepared by deposition-precipitation with urea. *Appl. Catal. B Environ.* **2013**, *140*, 363–377. [CrossRef]
24. Xu, Z.C.; Lai, E.C.; Shao-Horn, Y.; Hamad-Schifferli, K. Compositional dependence of the stability of AuCu alloy nanoparticles. *Chem. Commun.* **2012**, *48*, 5626–5628. [CrossRef] [PubMed]
25. Liu, X.Y.; Wang, A.Q.; Wang, X.D.; Mou, C.Y.; Zhang, T. Au–Cu Alloy nanoparticles confined in SBA-15 as a highly efficient catalyst for CO oxidation. *Chem. Commun.* **2008**, 3187–3189. [CrossRef] [PubMed]
26. Jeon, K.W.; Lee, D.G.; Kim, Y.K.; Baek, K.K.; Kim, K.; Jin, T.W.; Shim, J.H.; Park, J.Y.; Lee, I.S. Mechanistic insight into the conversion chemistry between Au–CuO heterostructured nanocrystals confined inside SiO_2 nanospheres. *Chem. Mater.* **2017**, *29*, 1788–1795. [CrossRef]
27. Carabineiro, S.A.C.; Bogdanchikova, N.; Avalos-Borja, M.; Pestryakov, A.; Tavares, P.B.; Figueiredo, J.L. Gold supported on metal oxides for carbon monoxide oxidation. *Nano Res.* **2011**, *4*, 180–193. [CrossRef]
28. Zhang, Z.J.; Wang, W.Z.; Shang, M.; Yin, W.Z. Low-temperature combustion synthesis of Bi_2WO_6 nanoparticles as a visible-light-driven photocatalyst. *J. Hazard. Mater.* **2010**, *177*, 1013–1018. [CrossRef] [PubMed]
29. Yu, C.L.; Bai, Y.; Chen, J.C.; Zhou, W.Q.; He, H.B.; Yu, J.C.; Zhu, L.H.; Xue, S.S. Pt/Bi_2WO_6 composite microflowers: High visible light photocatalytic performance and easy recycle. *Sep. Purif. Technol.* **2015**, *154*, 115–122. [CrossRef]
30. Zhang, G.Y.; Feng, Y.; Wu, Q.S.; Xu, Y.Y.; Gao, D.Z. Facile fabrication of flower-shaped Bi_2WO_6 superstructures and visible-light-driven photocatalytic performance. *Mater. Res. Bull.* **2012**, *47*, 1919–1924. [CrossRef]

31. Dittmer, A.; Menze, J.; Mei, B.; Strunk, J.; Luftman, H.S.; Gutkowski, R.; Wachs, I.E.; Schuhmann, W.; Muhler, M. Surface structure and photocatalytic properties of Bi_2WO_6 nanoplatelets modified by molybdena islands from chemical vapor deposition. *J. Phys. Chem. C* **2016**, *120*, 18191–18200. [CrossRef]
32. Cui, Y.M.; Li, H.Q.; Hong, W.S.; Fan, S.H.; Zhu, L.J. The effect of carbon content on the structure and photocatalytic activity of nano-Bi_2WO_6 powder. *Powder Technol.* **2013**, *247*, 151–160. [CrossRef]
33. Xie, H.D.; Shen, D.Z.; Wang, X.Q.; Shen, G.Q. Microwave hydrothermal synthesis and visible-light photocatalytic activity of Bi_2WO_6 nanoplates. *Mater. Chem. Phys.* **2007**, *103*, 334–339. [CrossRef]
34. Shang, M.; Wang, W.Z.; Ren, J.; Sun, S.M.; Wang, L.; Zhang, L. A practical visible-light-driven Bi_2WO_6 nanofibrous mat prepared by electrospinning. *J. Mater. Chem.* **2009**, *19*, 6213–6218. [CrossRef]
35. Wu, D.X.; Zhu, H.T.; Zhang, C.Y.; Chen, L. Novel synthesis of bismuth tungstate hollow nanospheres in water-ethanol mixed solvent. *Chem. Commun.* **2010**, *46*, 7250–7252. [CrossRef] [PubMed]
36. Ma, D.K.; Huang, S.M.; Chen, W.X.; Hu, S.W.; Shi, F.F.; Fan, K.L. Self-assembled three-dimensional hierarchical umbilicate Bi_2WO_6 microspheres from nanoplates: Controlled synthesis, photocatalytic activities, an wettability. *J. Phys. Chem. C* **2009**, *113*, 4369–4374. [CrossRef]
37. Wang, C.Y.; Zhan, H.; Li, F.; Zhu, L.Y. Degradation and mineralization of bisphenol a by mesoporous Bi_2WO_6 under simulated solar light irradiation. *Environ. Sci. Technol.* **2010**, *44*, 6843–6848. [CrossRef] [PubMed]
38. Lee, D.S.; Chen, Y.W. Au/CuO–CeO_2 catalyst for preferential oxidation of CO in hydrogen-rich stream: Effect of CuO content. *Int. J. Hydrog. Energy* **2016**, *41*, 3605–3612. [CrossRef]
39. Lei, J.H.; Liu, Y.; Wang, X.Y.; Hu, P.; Peng, X.S. Au/CuO nanosheets composite for glucose sensor and CO oxidation. *RSC Adv.* **2015**, *5*, 9130–9137. [CrossRef]
40. Konsolakis, M.; Carabineiro, S.A.C.; Papista, E.; Marnellos, G.E.; Tavares, P.B.; Moreira, J.A.; Romaguera-Barcelay, Y.; Figueiredo, J.L. Effect of preparation method on the solid state properties and the deN_2O performance of CuO-CeO_2 oxides. *Catal. Sci. Technol.* **2015**, *5*, 3714–3727. [CrossRef]
41. Carabineiro, S.A.C.; Bogdanchikova, N.; Tavares, P.B.; Figueiredo, J.L. Nanostructured iron oxide catalysts with gold for the oxidation of carbon monoxide. *RSC Adv.* **2012**, *2*, 2957–2965. [CrossRef]
42. Hu, Z.P.; Zhu, Y.P.; Gao, Z.M.; Wang, G.X.; Liu, Y.P.; Liu, X.Y.; Yuan, Z.Y. CuO catalysts supported on activated red mud for efficient catalytic carbon monoxide oxidation. *Chem. Eng. J.* **2016**, *302*, 23–32. [CrossRef]
43. Zhong, K.; Xue, J.J.; Mao, Y.C.; Wang, C.S.; Zhai, T.; Liu, P.; Xia, X.D.; Li, H.H.; Tong, Y.X. Facile synthesis of CuO nanorods with abundant adsorbed oxygen concomitant with high surface oxidation states for CO oxidation. *RSC Adv.* **2012**, *2*, 11520–11528. [CrossRef]
44. Liu, H.; Guo, K.; Duan, C.Y.; Chen, X.J.; Zhu, Z.F. A novel biosensor based on the direct electrochemistry of horseradish peroxidase immobilized in the three-dimensional flower-like Bi_2WO_6 microspheres. *Mater. Sci. Eng. C* **2016**, *64*, 243–248. [CrossRef] [PubMed]
45. Wang, L.L.; Huang, S.Y.; Zhu, B.L.; Zhang, S.M.; Huang, W.P. Preparation and characterization of mesoporous TiO_2-sphere-supported Au-nanoparticle catalysts with high activity for CO oxidation at ambient temperature. *J. Nanopart. Res.* **2016**, *18*, 323. [CrossRef]